

Magnetic and electronic ordering phenomena in the $[\text{Ru}_2\text{O}_6]$ honeycomb lattice compound AgRuO_3

Walter Schnelle,* Beluvalli E. Prasad,† Claudia Felser, and Martin Jansen
Max Planck Institute for Chemical Physics of Solids, 01187 Dresden, Germany

Evgenia V. Komleva and Sergey V. Streltsov
*M. N. Miheev Institute of Metal Physics of Ural Branch of Russian Academy of Sciences, 620137 Ekaterinburg, Russia and
Ural Federal University, Mira St. 19, 620002 Ekaterinburg, Russia*

Igor I. Mazin
*Department of Physics and Astronomy and Quantum Science and Engineering Center,
George Mason University, 22030 Fairfax, Virginia, USA*

Dmitry Khalyavin and Pascal Manuel
ISIS Neutron and Muon Source, Rutherford Appleton Laboratory, Didcot OX11 0QX, U.K.

Sukanya Pal, D. V. S. Muthu, and A. K. Sood
Department of Physics, Indian Institute of Science, Bangalore 560012, India

Ekaterina S. Klyushina and Bella Lake
*Helmholtz Zentrum Berlin für Materialien und Energie, 14109 Berlin, Germany and
Institut für Festkörperphysik, Technische Universität Berlin, 10623 Berlin, Germany*

Jean-Christophe Orain and Hubertus Luetkens
Laboratory for Muon-Spin Spectroscopy, Paul Scherrer Institute, 5232 Villigen PSI, Switzerland
(Dated: March 9, 2021)

The silver ruthenium oxide AgRuO_3 consists of honeycomb $[\text{Ru}_2^{5+}\text{O}_6^{2-}]$ layers, and can be considered an analogue of SrRu_2O_6 with a different intercalation stage. We present measurements of magnetic susceptibility and specific heat on AgRuO_3 single crystals which reveal a sharp antiferromagnetic transition at 342(3) K. The electrical transport in single crystals of AgRuO_3 is determined by a combination of activated conduction over an intrinsic semiconducting gap of ≈ 100 meV and carriers trapped and thermally released from defects. From powder neutron diffraction data a Néel-type antiferromagnetic structure with the Ru moments along the c axis is derived. Raman and muon spin rotation spectroscopy measurements on AgRuO_3 powder samples indicate a further weak phase transition or a crossover in the temperature range 125–200 K. The transition does not show up in magnetic susceptibility and its origin is argued to be related to defects but cannot be fully clarified. The experimental findings are complemented by DFT-based electronic structure calculations. It is found that the magnetism in AgRuO_3 is similar to that of SrRu_2O_6 , however with stronger intralayer and weaker interlayer magnetic exchange interactions.

I. INTRODUCTION

Ruthenium and its compounds feature impressively diverse chemical and physical phenomena. This is reflected, for instance, by the oxidation states accessible within the wide span from -2 to $+8$ and by particular electronic and magnetic ground states formed in molecular compounds as well as in extended solids. This is especially relevant in condensed matter research, where ruthenium oxides and chlorides continue to attract prominent attention. Accessibility of different valence states of Ru results in a dramatic variability of physical properties even within

the small structural motif. Indeed, honeycomb $\text{Ru}^{3+}L_3$ layers (L = ligand atom) form one of the cleanest Kitaev system known so far, with strong bond-dependent anisotropic exchange [1, 2], $\text{Ru}^{4+}L_3$ dimerizes at low temperatures and forms a unique covalent bond liquid above 270°C [3]. In the compound SrRu_2O_6 , $\text{Ru}^{5+}L_3$ was argued to feature unusual quasimolecular orbitals (QMO), which determine the suppression of the magnetic moment and robust antiferromagnetic (AFM) coupling [4, 5].

In different structural contexts Ru^{4+} is noted for other unique physical phenomenon. For example, the dioxide RuO_2 was recently shown to be an example of a novel magnetic state of matter, an antiferromagnet without Kramers degeneracy, with unique physical ramifications [6]. It also generates a series of perovskite compounds ranging from SrRuO_3 , CaRuO_3 and BaRuO_3 , all bad metallic, ferromagnetic or nearly-ferromagnetic, with a

* walter.schnelle@cpfs.mpg.de

† Now at Department of Chemistry, RV Institute of Technology and Management, Bangalore, 560076, India

strong effect of magnetic fluctuations on transport [7–9], to $\text{Sr}_3\text{Ru}_2\text{O}_7$ featuring one of the first experimentally observed magnetic quantum critical points, and Sr_2RuO_4 , an enigmatic material for many years misidentified as spin-triplet superconductor [10, 11].

The recently synthesized AgRuO_3 [12] (space group $R\bar{3}c$, $a = 5.2261(6)$ Å, $c = 32.358(5)$ Å, $Z = 12$) featuring $\text{Ru}^{5+} 4d^3$ species comes close to the conception of a 2D material [13], in as much it consists of stacked honeycomb $[\text{Ru}_2\text{O}_6]$ poly-oxoanions, where the empty octahedral sites are capped from both sides with silver atoms. Thus, the resulting $(\text{Ag}_2\text{Ru}_2\text{O}_6)_n$ slabs are charge neutral and resemble giant molecules. Based on magnetic susceptibility measurements on a powder sample and a preliminary evaluation of time of flight (TOF) neutron diffraction data it was claimed that AgRuO_3 would show strong magnetic exchange coupling, however, no long range magnetic order could be detected at that time [12], while in seeming contradiction with the experiment first-principle calculations were predicting AgRuO_3 to be magnetically very similar to SrRu_2O_6 (supporting information for Ref. [12]). The latter has been investigated intensively – experimentally and theoretically – in the last years [4, 14–23] and was shown to have the transition to a Néel AFM groundstate at ≈ 560 K. Moreover, in 2019 also BaRu_2O_6 was synthesized which appears to have a related crystal structure [24].

Here, we present detailed measurements of the magnetic susceptibility, electrical resistivity, specific heat and Raman spectroscopy on AgRuO_3 single crystals and high-resolution TOF neutron data and muon spin rotation spectroscopy (μSR) data on polycrystalline material, all clearly demonstrating the presence of long-range AFM order up to $\approx 342(3)$ K. This relatively high Néel temperature of AgRuO_3 is in agreement with our first principles analysis of the electronic structure. In several respects AgRuO_3 parallels the properties of SrRu_2O_6 , however, there are conspicuous differences. Specifically, there is a change of regime, possibly a second phase transition, around 125–200 K within the AFM phase. It does not show up in either magnetic susceptibility or specific heat, but there are clear changes in both μSR and Raman spectra in this range, and, in roughly the same range, the resistance shows nontrivial and nonmonotonic temperature behavior which can be explained by defect states.

In this paper we first present the extensive experimental findings, then complement them with the electronic structure results, and finally sum up relevant implications. While the Néel transition at 342 K can be well described in terms of quasi-2D magnetic interactions resulting from the first principles calculation and QMOs, the nature of the low-temperature phase transition(s) or crossover is probably related to defect states, but remains not fully clarified.

II. EXPERIMENTAL AND CALCULATION DETAILS

For the measurements of various physical properties we used either portions of, or selected sets of tiny single crystals from the large polycrystalline sample of AgRuO_3 that had been synthesized as previously described [12].

Magnetization was measured on a set of 10 selected single crystals (total mass 622 μg) with a MPMS3 (SQUID-VSM, Quantum Design) magnetometer. The crystals were glued with a minute amount of GE varnish to a quartz sample holder with the c axes oriented either parallel or perpendicular to the applied field. Data were measured on warming after zero-field cooling (zfc) and on cooling (fc) in different magnetic fields.

Electrical resistance was determined on several crystals with a four probe ac method (RES option, PPMS9, Quantum Design). Contacts in the hexagonal a plane of the crystals ($I \perp c$) or at the bases of short prismatic crystals ($I \parallel c$) were made with Pt wires (25 μm) and silver paint. The geometry factors could not be determined reliably (for resistivity data on a polycrystalline sample see Fig. 2 of Ref. [12]).

Heat capacity up to 300 K was measured on a cold-pressed pellet with the HC option of a PPMS9 (Quantum Design) in magnetic fields up to $\mu_0 H = 9$ T. Above 300 K the melting of the thermal contact agent (high vacuum grease Apiezon N) lead to unreliable results. Therefore, additional heat capacity data were obtained with a differential scanning calorimeter (DSC; PerkinElmer DSC8500) at heating rates of 5 and 20 K min^{-1} .

Neutron diffraction measurements were performed at the ISIS pulsed neutron and muon facility of the Rutherford Appleton Laboratory (UK), on the high-resolution cold-neutron diffractometer WISH located at the second target station [25]. Polycrystalline AgRuO_3 (≈ 2 g) was loaded into a cylindrical 6 mm diameter vanadium can and measured on warming using an Oxford Instruments cryostat and a CCR hot-stage, respectively. Rietveld refinement of the crystal structure was performed using the FullProf program [26] against the data collected in detector banks at average 2θ values of 58°, 90°, 122°, and 154°, each covering 32° of the scattering plane.

Temperature dependent Raman spectroscopy experiments were carried out on crystals using a Linkam THMS350V in the range of 77 K to 385 K. The sample was cooled with a continuous flow of liquid nitrogen. Raman spectra were recorded in a LabRam spectrometer (Horiba) in back-scattering geometry, using a 50 \times objective and laser excitation of 532 and 660 nm.

Zero-field (ZF) $\mu^+\text{SR}$ (μSR) measurements of polycrystalline AgRuO_3 were performed using Dolly and GPS muon spectrometers at the Swiss Muon Source. For the measurements 1.8 g of powder AgRuO_3 was pressed into a pellet and mounted on a silver sample holder. The measurements were performed over the temperature ranges $0.2 \text{ K} < T < 65 \text{ K}$ using an Oxford Heliox and $65 \text{ K} < T < 295 \text{ K}$ in an Oxford Variox cryostat.

The crystal structure for the electronic structure calculations was taken from Ref. [12]. The band structure calculations were performed using the Wien2k [nonmagnetic GGA (Generalized Gradient Approximation)], including Wannier function projections [27] and Vienna Ab-initio Simulation Package (VASP, all magnetic calculations) [28]. We utilized the projector augmented-wave (PAW) method [29] with the Perdew-Burke-Ernzerhof (PBE) GGA functional [30]. The energy cutoff chosen in VASP was $E_{\text{cutoff}} \sim 600$ eV and the $6 \times 6 \times 6$ Monkhorst-Pack grid of k points was used in the calculations.

III. RESULTS

A. Magnetism

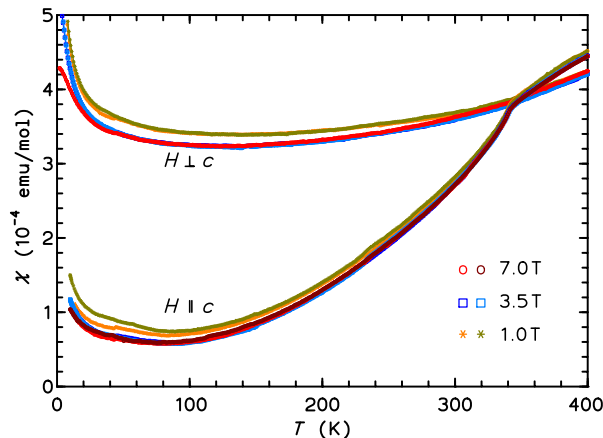


FIG. 1. Magnetic susceptibility $\chi(T)$ of AgRuO_3 crystals measured in three different fields parallel and perpendicular to the crystallographic c axes of the crystals. Light color symbols = zfc, dark color symbols = fc protocol. Except for the lowest temperatures the zfc and fc curves coincide. Also the data for 3.5 T and 7.0 T coincide over large temperature intervals.

The magnetic susceptibility of AgRuO_3 up to 400 K is shown in Fig. 1. Generally, the molar susceptibility is small. Above $T = 20$ K it is only weakly dependent on the applied field and the zfc and fc protocol data almost coincide. For $H \parallel c$ the susceptibility χ_{\parallel} displays a sharp kink at $T_N = 342$ K, below which χ_{\parallel} strongly decreases. $\chi_{\perp}(T)$ shows a weak temperature dependence and a very weak kink at the same temperature (the slope is larger above T_N). Interestingly, the values of χ_{\parallel} and χ_{\perp} coincide at T_N but at $T = 90$ K the anisotropy $\chi_{\perp}/\chi_{\parallel} \approx 6$. These findings suggest an AFM order with the Ru moments aligned along the c axis. Up to our maximum field of 7 T the magnetization data show no indication for a spin-flop or other metamagnetic transition.

Well below the ordering temperature, $\chi(T)$ for both directions show a weak upturn, which we attribute to Curie-paramagnetic impurities or charged defects in the

sample. An estimate can be made by fitting a Curie law $C/T + \chi_0$ to the 1.0 T data for $H \parallel c$ from 10–100 K. C corresponds to $0.10 \mu_B$, equivalent to 0.3% of spin 1/2 magnetic species. It should be mentioned that in measurements on loose powder samples (cf. Fig. 3 in Ref. [12]) preferential alignment of the crystallites along the easy axis can occur at high applied fields (typically $\mu_0 H \geq 1$ T). In measurements on powders in low applied fields no phase transitions or indications for a weak ferromagnetic component of the AFM order were detected.

B. Electrical transport

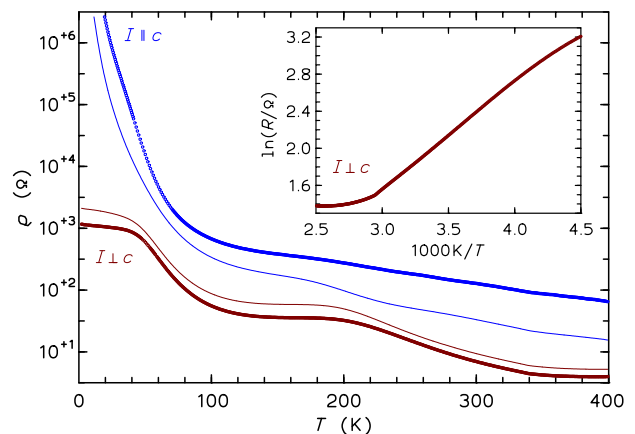


FIG. 2. Electrical resistance $R(T)$ of selected AgRuO_3 crystal for current in the hexagonal a plane ($I \perp c$) and current along the c axis ($I \parallel c$). The inset shows an Arrhenius-type plot of the in-plane resistance data. The thick and thin lines represent the data for two typical samples.

The temperature dependence of the electrical resistance was measured on several single crystals. The characteristics of the resistance curves measured with current in the a plane ($I \perp c$) are well reproduced on several crystals (Fig. 2, red curves). With decreasing temperature the resistance generally increases and at $T_N \approx 340$ K a change to a steeper slope (activated conduction, cf. inset of Fig. 2) can be observed. A plateau-like behavior is seen between ≈ 190 K and ≈ 130 K, below which the resistance starts to rise again. Finally, the in-plane resistance appears to reach another plateau below $T < 30$ K. This characteristic behavior is in stark contrast to the c axis resistance (Fig. 2, green curves), which is roughly one order of magnitude higher and increases continuously with decreasing temperature, seemingly indicating a different activated conduction behavior. At $T \approx 130$ K a changeover to a much stronger slope is observed. It has to be mentioned that not all crystals showed such high resistance at low T (compare the two green curves in Fig. 2), which can be rationalized by the poor mechanical quality of the specimens. For all crystal a weak kink is visible in the a plane resistance at the Néel temperature.

In order to get a better insight, we have calculated the function $E_g(T) = -k_B T^2 (d \ln \rho / dT)$ (Fig. 3). For both directions the activation barrier shows a profound temperature dependence, by no means attributable to a single gap. The high- T behavior is consistent with an activation gap of the order of 0.07–0.09 eV for the both directions. The apparent gap drops nearly to zero around at $T \sim 150$ K (170 K), for the c (a) directions, and raises again upon cooling to ~ 55 K (75 K) to the values of ~ 0.035 (0.025) eV, respectively. Then it drops to zero again as $T \rightarrow 0$.

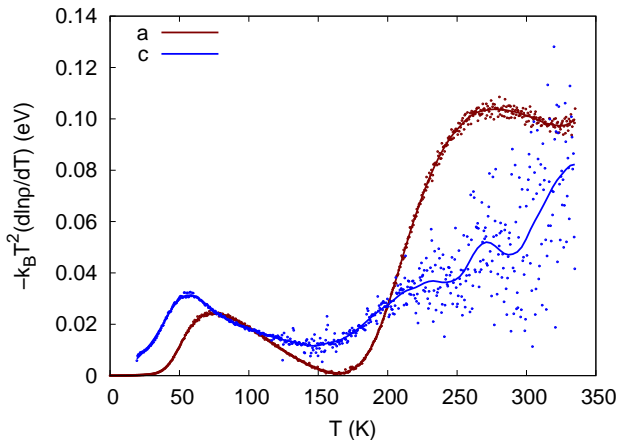


FIG. 3. Effective transport excitation gap defined as $E_g(T) = -k_B T^2 (d \ln \rho / dT)$ for current in the a plane and along the c axis. The continuous lines are spline-smoothed data.

While the temperature dependence of the derivative-deduced activation energy is qualitatively similar in both directions, the details are very different. Since the actual gap is a scalar quantity, the only way to reconcile this observation is to assume that there are several different reservoirs of the current carriers, one of them corresponding to the actual excitation gap, with should be larger that ~ 0.1 eV, and the other(s) representing various defect states inside the gap. A very small number of carriers are actually metallic, and are responsible for the $T \rightarrow 0$ limit of the activation energy. In addition, there are defect states that carry a small number of carriers, and start to donate carriers at around 50 K, but get depleted at higher temperature. A closer inspection shows that one also needs to introduce temperature dependent scattering, presumably related to the same defect states and determined by a similar activation energy. Note that the defect-derived carriers dominate the low- T regime, while the high temperature transport is effected by the carrier thermally excited across the fundamental gap. With this in mind, we tried to fit the conductivity $\sigma = 1/\rho$ with:

$$\begin{aligned} \sigma &= n\tau \\ n &= n_1 \exp(-E_g/T) + \frac{n_2}{(1 + \exp(D/T))} \\ 1/\tau &= 1/\tau_0 + \frac{1/\tau_1}{(1 + \exp(D'/T))} \end{aligned} \quad (1)$$

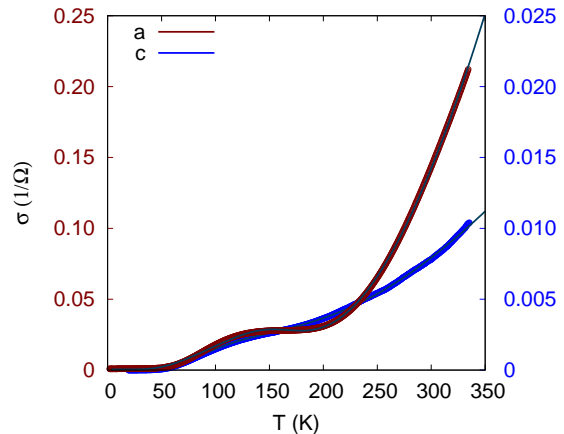


FIG. 4. Fitting to Eq. 2 (lines) of the experimental conductivity data (circles). The left (red) scale corresponds to the a -plane, the right (blue) scale to the c -axis conductivity.

As shown in Fig. 4 this provides a perfect fit to the data, although the parameters differ between the two directions. While the fit is not very sensitive to the parameters D and D' s and they can be forced to be the same, with only moderate loss of the fit quality, the fundamental gap E_g is important for getting the high-temperature resistance right. We can only conclude that the transport in the c direction is contaminated by grain boundaries and other defects, or is plainly not Boltzmannian. The exceptionally large transport anisotropy is suggestive of that. The formula (simplified in the sense that all defect states are lumped together into a single level) is

$$\sigma = \frac{\sigma_0 + \sigma_1 \exp(-E_g/T) + \sigma_2 / (1 + \exp(D/T))}{1 + A / (1 + \exp(D'/T))} \quad (2)$$

The parameters derived from the a plane transport are: $\sigma_0 = 5 \times 10^{-4}$, $\sigma_1 = 9 \times 10^3$, $\sigma_2 = 0.2 \Omega^{-1}$, $E_g = 200$ meV, $D = 20$ meV, $D' = 115$ meV, $A = 1300$. As mentioned, D' can actually be set to be the same as D with only moderate deterioration of the fit. For the c axis these numbers are $\sigma_0 = 9 \times 10^{-8}$, $\sigma_1 = 2.1$, $\sigma_2 = 0.08 \Omega^{-1}$, $E_g = 110$ meV, $D = 30$ meV, $D' = 30$ meV, $A = 20$, but these numbers should be taken with a huge grain of salt.

One take-home message is that a defect level located at 20–30 meV (corresponding, roughly, to $T \sim 200$ –300 K) is capable of generating the anomaly in temperature dependence of transport, visually located at 150–170 K.

C. Specific heat

The specific heat is shown in Fig. 5a in a c_p/T vs. T representation. In the covered temperature range no peak or anomalous broadened feature can be seen, suggesting the absence of any phase transition in this temperature range. The data in the low temperature range (Fig. 5b) are well described by $c_p(T) = \gamma'T + \beta T^3 + \delta T^5$ with the latter two terms describing the phonon contribution. The fit results in $\beta = 0.913(3)$ mJ mol⁻¹ K⁻⁴, corresponding to the initial Debye temperature of 220 K, and $\delta = -0.00060(1)$ mJ mol⁻¹ K⁻⁶ the next term in the harmonic lattice approximation constituting a small correction. The linear coefficient $\gamma' = 5.6(1)$ mJ mol⁻¹ K⁻² is quite large (there should be no conduction electron term). It is probably due to a rather high concentration of point defects. It appears that the majority of these defects does not show up as an upturn of the magnetic susceptibility towards low T (cf. Fig. 1), thus they should be predominantly nonmagnetic, e.g. oxygen or silver defects. The magnetic field dependence of $c_p(T)$ up to 9 T is very weak.

The DSC specific heat data (Fig. 5c) around room temperature are about 5% higher than the PPMS data and have realistic values close to the Dulong-Petit limit ($c_p \approx 3nR$, where $n = 5$ is the number of atoms and R the gas constant). They display a clear second-order-type anomaly with a midpoint at $T_N \approx 344$ K, corroborating the long-range magnetic order at that temperature. No heating rate dependence of $c_p(T)$ or latent heat is observed. We assign this transition to the AFM long-range ordering of the Ru moments.

D. Neutron diffraction

To further confirm the presence of long-range magnetic ordering, neutron diffraction measurements ($1.5 \text{ K} < T < 348 \text{ K}$) were performed. The data revealed that some of the reflections demonstrate a strong temperature dependence below $T_N \approx 335 \text{ K}$ (Fig. 6c, inset), which is consistent with the fact that magnetic unit cell coincides with the cell of the nuclear structure and the subsequent refinement of the diffraction patterns (see, e.g., Fig. 6b) was done assuming zero magnetic propagation vector ($k = 0$).

The refinement was assisted by symmetry arguments based on the representation theory [31, 32] and the parametrization for the magnetic form factor of Ru⁵⁺ has been taken from Ref. [33]. It has been found that a simple magnetic structure with antiparallel alignment of spins on the nearest neighbor Ru sites (Néel structure) provides a good refinement quality of the neutron diffraction data (Fig. 6b) in the whole temperature range below T_N . Surprisingly, the fitting quality was found to be almost insensitive to the moment direction, complicating the choice between the models with in-plane and out-of-plane spin polarization. However, our DFT calculations that take into account spin-orbit coupling (see the Sec.

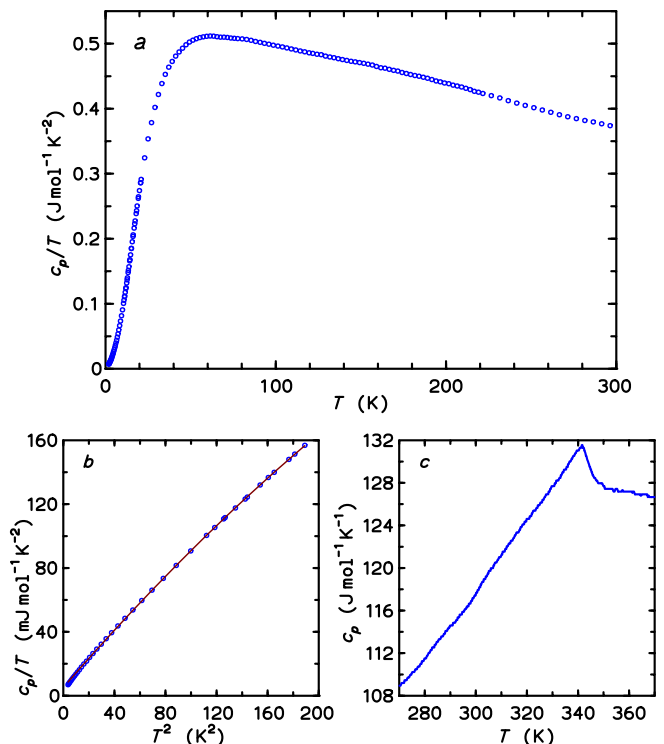


FIG. 5. (a) Specific heat of AgRuO₃. (b) low-temperature data in the c_p/T vs. T^2 representation. The line is the fit as detailed in the text (c) high-temperature differential scanning calorimetry data (DSC; scan rate 20 K min⁻¹).

III G for details) strongly support the model with out-of-plane spin orientation, in agreement with the observed anisotropy of the magnetic susceptibility. Note that this spin direction was also found experimentally in another trigonal ruthenate, SrRu₂O₆ [15, 23].

The magnetic structure of AgRuO₃ (Fig. 6a) implies $\bar{R}3'c'$ magnetic symmetry with the ordered moment size of $1.85(5) \mu_B$ at $T = 1.5 \text{ K}$. The moment varies smoothly with temperature (Fig. 6c) indicating that the anomalous behavior found between 170 and 225 K in the Raman and μ SR measurements is likely to be predominantly nonmagnetic in origin.

E. Raman spectroscopy

Raman scattering has the ability to identify the role of phonons in structural and magnetic transitions, the latter via spin-phonon coupling. At ambient temperature AgRuO₃ has a trigonal $R\bar{3}c$ structure with 25 Raman active modes of A_{1g} and E_g symmetries. Figure 7 shows the reduced Raman susceptibility $\chi''(\omega) = I(\omega)/(n(\omega) + 1)$, where $I(\omega)$ is the observed intensity and $[(n(\omega) + 1)]$ is the Bose-Einstein factor, at a few typical temperatures. Lorentzian line shapes were fitted to $\chi''(\omega)$ to extract the phonon frequencies, full width at half maximum (FWHM), and integrated intensities of the Ra-

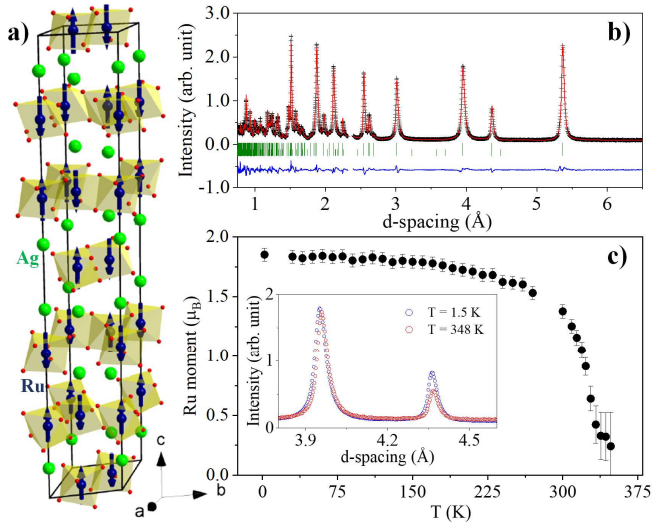


FIG. 6. (a) Schematic representation of the magnetic structure of AgRuO₃ with the $\bar{R}3'c'$ magnetic space group. (b) Rietveld refinement of the neutron diffraction pattern collected at $T = 1.5$ K ($R_{\text{nuclear}}^{\text{Bragg}} = 2.66\%$ and $R_{\text{magnetic}}^{\text{Bragg}} = 3.2\%$). (c) Ru ordered moment versus temperature. The inset shows two peaks of the neutron diffraction patterns collected at different temperatures.

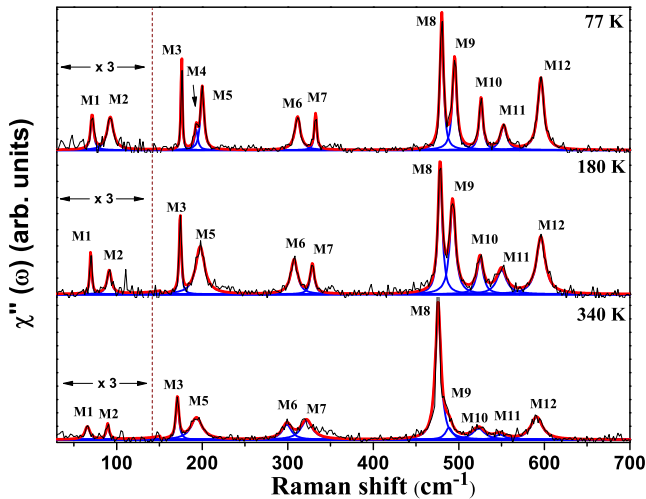


FIG. 7. Raman spectra of AgRuO₃ at typical temperatures (black lines). The solid red line is a Lorentzian fit to the data, blue solid lines are individual fits of the Raman modes. The arrow indicates the additional mode M4.

man modes. Table 1 in the Supplemental Material [34] lists the experimentally (at 300 K) observed and calculated frequencies for the trigonal high-temperature (HT) AFM state, which are shown with the corresponding error bars (for an explanation of how the error bars were decided for the theoretical values, see Ref. [34]). The agreement is nearly perfect. At 77 K, twelve first-order Raman modes (M1 to M12) are observed in the spectral range 30–650 cm⁻¹. Most noticeable is the disappear-

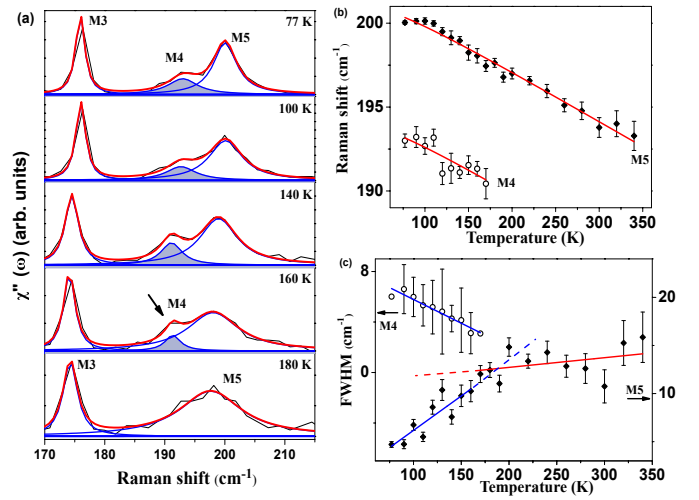


FIG. 8. (a) Temperature evolution of the Raman spectra in the range 170–220 cm⁻¹. The solid red line is a Lorentzian fit to the data, blue solid lines are individual fits of the Raman modes. The (b) Raman shift and (c) FWHM of the modes M4 and M5 plotted as a function of temperature. The red lines are fit to the anharmonic model and blue lines are linear fits to the data.

ance of mode M4 above 170 K, while all other modes are present in our working temperature range.

To bring home this point clearly, Fig. 8a presents the fitted Raman spectra for selected temperatures in the spectral range 170–225 cm⁻¹. The temperature evolution of the mode frequencies and FWHM for modes M4 and M5 are shown in Fig. 8b and 8c, respectively. The FWHM of the mode M4 is anomalous, i.e. it increases as temperature is lowered. The FWHM of the mode M5 also shows a significant change at 170 K. The temperature dependence of the frequencies and linewidths of the remaining phonons is given in the Supplemental Material, Fig. 1 and Fig. 2 [34], respectively. Phonon frequencies show the expected behavior of decreasing frequency as T is increased due to quasi-harmonic (i.e. thermal expansion effect) and anharmonic effects [35]. The solid red lines are fits to the simple cubic anharmonic model where a phonon decays into two phonons of equal frequencies [35], given by $\omega^{\text{cubic}}(T) = \omega(0) + C[1 + 2n(\omega(0)/2)]$, C being the self-energy parameter. Coming back to mode M4, it is clearly visible for both polarizations at $T = 77$ K (see Fig. 3 of the Supplemental Material [34]) but disappears at around 170 K. Fig. 9a shows the integrated intensity of this mode as a function of T . Given the error bars, this dependence is equally well consistent with a linear behavior (shown), with an exponential decay in the entire temperature range, or a square-root dependence corresponding to a second order phase transition at $T_c = 170$ K (both not shown).

Further, as shown in Fig. 9b, the intensity of mode M9 normalized with respect to mode M8 shows a distinct change at 170 K. The intensity of M9 gradually decreases with T and goes to zero near the AFM or-

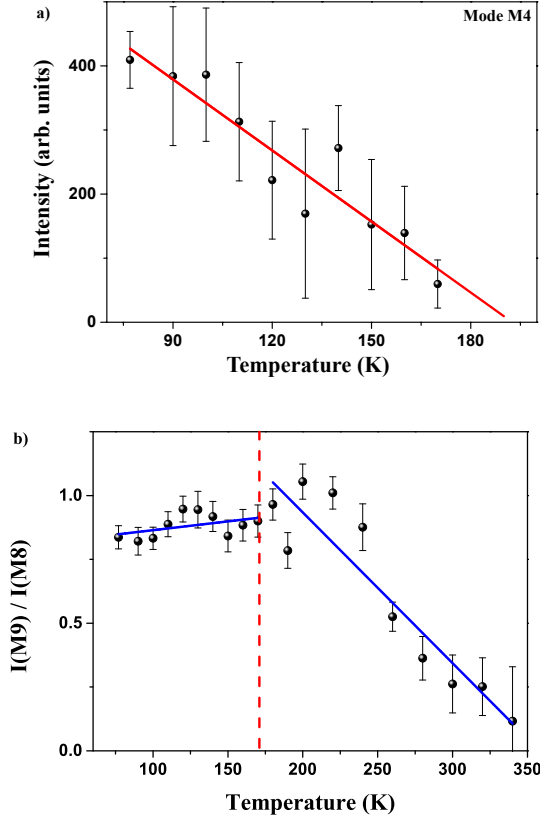


FIG. 9. (a) Temperature evolution of the integrated intensity of the M4 Raman mode. The red line is a linear fit resulting in an intercept $T_c = 193(5)$ K. (b) The ratio of integrated intensities of mode M9 to M8 shows a change in slope around 170 K. The blue solid lines are linear fits to the data below and above 170 K.

dering temperature T_N . All these observations of distinct changes in temperature dependence of the phonon modes M4, M5 and M9 indicate subtle structural changes around $T \approx 170$ K. However, absence of any distinct feature at this temperature in other probes suggest that these changes do not constitute a true phase transition, but indicate a crossover region probably stretching between 150 and 200 K. Note that this is the same range where the in-gap defect states strongly affect electrical transport, albeit a mechanism by which free carriers dominated by these states can affect the Raman scattering is not clear.

We now come to the higher spectral range shown in Fig. 10a where we observe a weak broad band at 1155 cm^{-1} . To establish that this is a Raman mode and not photoluminescence, we did experiments at 77 K with two different incident photon excitations, 660 nm and 532 nm (shown with the thick green line in Fig. 10a). This confirms that the mode at $\approx 1155 \text{ cm}^{-1}$ is a Raman mode. Fig. 10b shows the temperature dependence of the integrated intensity of this broad band. The red line (a linear fit) is intended as a guide to the eye.

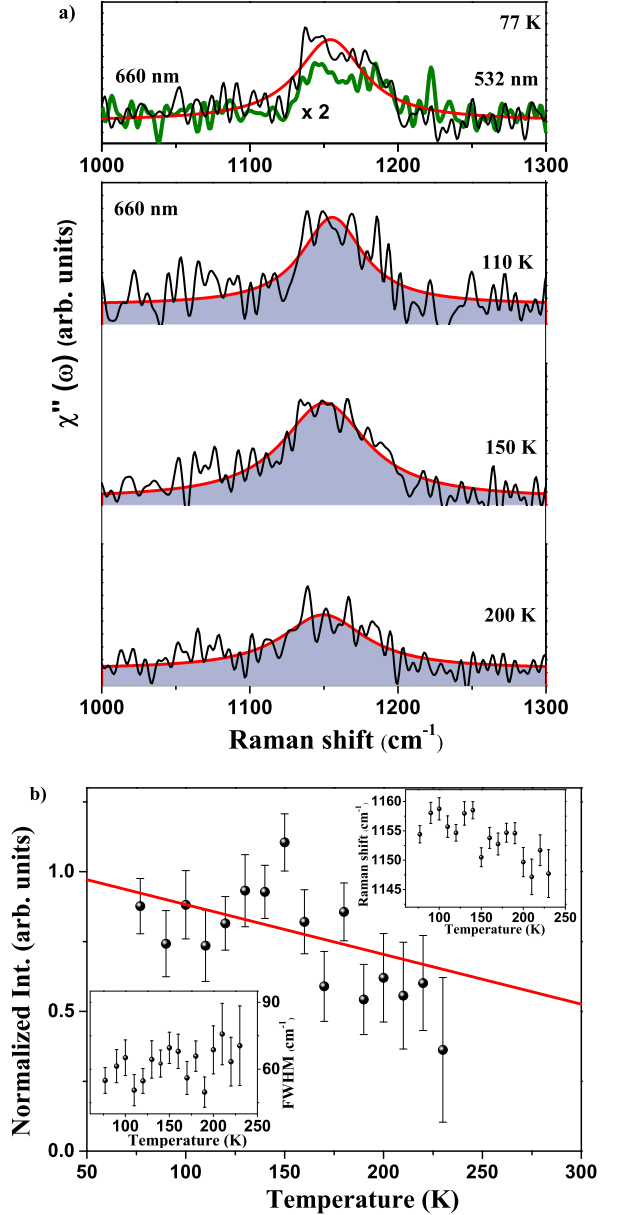


FIG. 10. (a) The broad mode is observed with both 532 nm (shown by solid thick green line) and 600 nm lasers at 77 K. Temperature evolution of the broad mode of with 660 nm red laser is shown subsequently. Raw data (high frequency noise has been filtered out). The red lines are Lorentzian lineshape fits. (b) Temperature dependence of the intensity of the broad mode. The red solid line is a linear fit to the data. The frequency and the linewidth as a function of temperature are shown in the insets.

The T -dependence of the frequency and the linewidth are shown in the insets of Fig. 10b. In several Heisenberg antiferromagnets, like in $\text{YBa}_2\text{Cu}_3\text{O}_6$ [36], Sr_2IrO_4 , $\text{Sr}_3\text{Ir}_2\text{O}_7$ [37], and SrRu_2O_6 [20] two-magnon Raman modes have been observed in the magnetically ordered

state. If the Heisenberg model is defined as

$$H = \sum_{i \neq j} J_{ij} \mathbf{S}_i \mathbf{S}_j, \quad (3)$$

then the frequency of two-magnon Raman scattering is $\sim 17J$. [20]. Taking $s = 1$ we get an estimate of $J \approx 97$ K, close to our calculated value (see Sec. III G below).

However, we cannot completely rule out the possibility of electronic Raman scattering associated with the electronic transition between the QMOs of Ru^{5+} , as in the case of SrRu_2O_6 [5], although, in principle, one would expect such transitions to manifest at higher energies.

F. Muon spin rotation spectroscopy

Figure 11c shows the time-dependence of the muon spin polarization in AgRuO_3 measured on the DOLLY spectrometer at the base temperature of $T = 0.2$ K in zero field (ZF). The modulated oscillations indicate the presence of an internal magnetic field in the sample due to long-range magnetic order. The Fast Fourier transformation (FFt) of the data (Fig. 12) shows that, in general, there are two fractions of the muon spin ensemble which oscillate with different frequencies giving rise to two peaks ≈ 17 and ≈ 23 MHz. The presence of two frequencies can be attributed to two magnetically and/or crystallographically inequivalent muon stopping sites in the crystal structure. To extract the frequencies of the observed oscillations, the ZF- μ SR spectrum at $T = 0.2$ K was analyzed with the software package MUSRFIT [38] using the fitting function:

$$A(t) = \sum_{i=1}^2 A_i \cos(2\pi\nu_i t) \exp(-\lambda_i t) + A_3 \exp(-\lambda_3 t) \quad (4)$$

Here, A_1 and A_2 are the amplitudes of the muon spin oscillations due to the component of the internal field which is perpendicular to the muon spin polarization; ν_1 and ν_2 are the frequencies of these oscillations which are connected to the internal field via the relation $\nu_i = \gamma_\mu |B_i| / 2\pi$ where γ_μ is the muon gyromagnetic ratio and $|B_i|$ are the averaged internal fields on the two stopping sites. The exponential terms describe the damping of the oscillation with relaxation rates λ_1 and λ_2 and assume a Lorentzian field distribution. The amplitude A_3 and the corresponding relaxation rate λ_3 take into account a contribution of nonoscillatory signal due to the interaction of the muons with the internal fields which are parallel to the initial muon spin polarization. The best fit was achieved for the frequencies of $\nu_1 = 17.074 \pm 0.006$ MHz and $\nu_2 = 23.456 \pm 0.003$ MHz at $T = 0.2$ K which correspond to local fields of 1.26 T and 1.3 T respectively. Furthermore, the harmonic form of the oscillations indicates that the long-range magnetic order in the ground state of AgRuO_3 is commensurate.

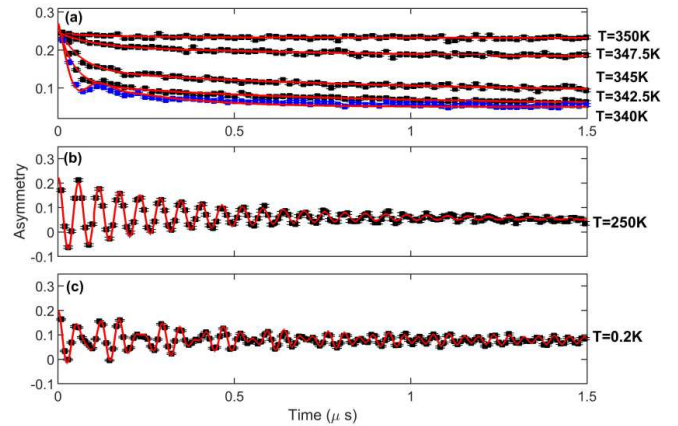


FIG. 11. Zero-field μ SR spectra measured on powder AgRuO_3 at (a) $T = 342.5, 345, 347.5$ and 350 K using the GPS muon spectrometer; (b) $T = 250$ and (c) $T = 0.2$ K using the Dolly spectrometer. The red lines represent the best results of the fit analysis described in the text.

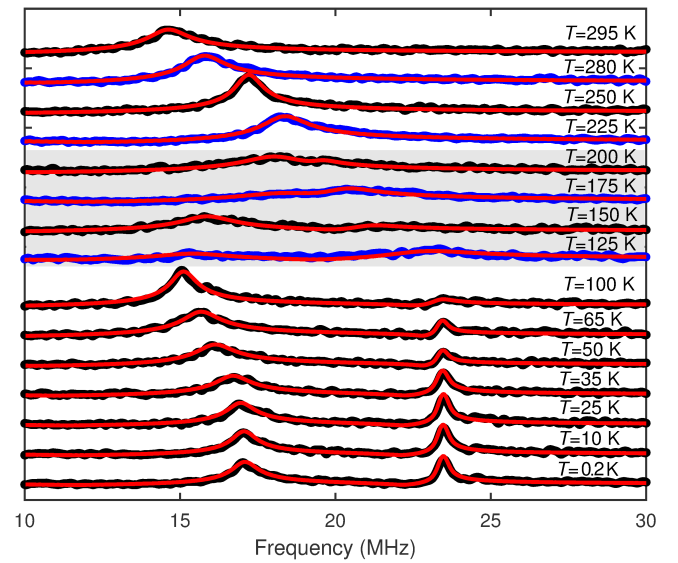


FIG. 12. Fast Fourier transformation of the muon spin-precession signal measured in zero-field at various temperatures using the Dolly (black) and GPS (blue) spectrometers. The FFt of the best fit to Eq. 4 is given by the red lines through the FFt data. The gray area indicate the temperature regime $125 \text{ K} \leq T \leq 200 \text{ K}$.

Further ZF- μ SR measurements were performed using DOLLY and GPS spectrometers to explore the temperature dependence of the harmonic modes observed at base temperature. Figure 12 shows the evolution of the FFt of ZF- μ^+ SR spectra collected up to 295 K. The frequencies of the oscillations in the ZF- μ^+ SR spectra correspond to the peaks in the FFt. The solid red lines represent the FFt of the best fit of the data achieved using Eq. 4. As Fig. 12 shows, there are three different temperature regimes: (i) $T < 125$ K, (ii) $125 \text{ K} \leq T \leq 200$ K and (iii) $T > 200$ K. Below ~ 125 K, there are two distinct and

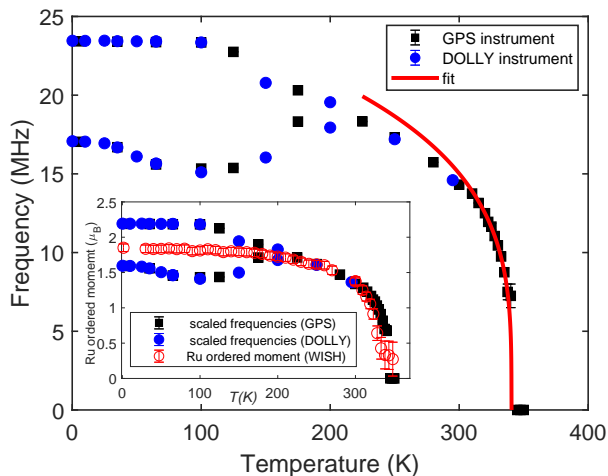


FIG. 13. Temperature dependence of the muon-spin precession frequencies extracted from the analysis of ZF- μ SR spectra of AgRuO₃. Blue circles and black squares correspond to the frequencies extracted from the muon data collected at the Dolly and GPS spectrometers, respectively. The red line gives the best fit achieved using Eq. 6. The inset shows a comparison of the scaled ZF- μ SR frequencies (blue circles and black squares) with the Ru ordered moment (red circles) from neutron diffraction data.

well-defined frequencies, the lower one noticeably softening with temperature, from ≈ 17 MHz at $T = 0.2$ K to ≈ 15 MHz at $T = 100$ K. The other one is basically T -independent, at $\nu \approx 23.5$ MHz. Between $T = 125$ and 200 K the spectra are extremely broad with some traces of one or possibly two frequencies within the range $\nu \approx 16$ MHz and $\nu \approx 25$ MHz. Furthermore, the relative intensity and widths (but not frequencies!) of the spectral features in this range is very sample-dependent (note that the sample used on the two different instruments were from different batches), indicating a possible role of impurities. A single sharp frequency which is sample independent reappears at ≈ 17 MHz for $T = 225$ K, and is clearly visible at $T = 295$ K, at ≈ 15 MHz. The extracted frequencies are plotted as a function of temperature in Fig. 13. The points between 125 K and 200 K where the FFT of the signal is unclear give our the best guesses of the possible position of two peaks in FFT while below 125 K two clear frequencies are observed.

Intriguing, the enigmatic intermediate temperature regime spans the same region where the Raman spectra undergo qualitative changes and the differential resistance is positive. It is possible that all three phenomena have the same origin. The resistance analysis and the temperature-selective μ SR spectra suggest that charge dynamics related to defect traps may be relevant.

To explore the higher temperature regime, where a single frequency was observed, the ZF- μ SR spectra of AgRuO₃ were collected on the GPS spectrometer over the temperature range $300 \text{ K} < T < 350 \text{ K}$ with step in temperature of 5 K and 2.5 K. The data were analyzed

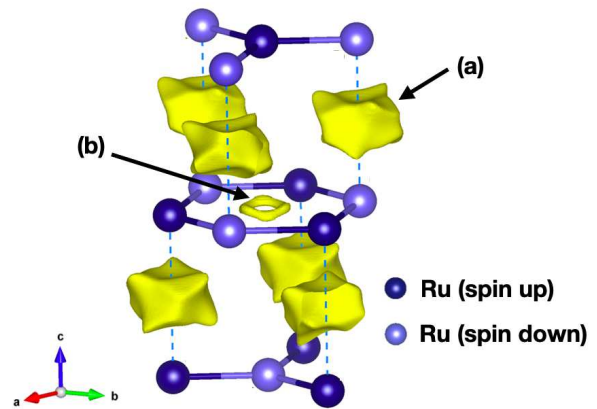


FIG. 14. Electrostatic potential in the antiferromagnetically ordered AgRuO₃, showing the potential muon trapping sites (yellow). The Ru atoms (purple) and some outlines of the $R\bar{3}c$ crystallographic unit cell are shown.

using the function:

$$A(t) = F_m [A_0 \cos(2\pi\nu_0 t) \exp(-\lambda_0 t) + A_3 \exp(-\lambda_3 t)] + (1 - F_m)G_{KT} \quad (5)$$

where F_m is the fraction of the magnetically ordered state. This function includes a Kubo-Toyabe term G_{KT} which takes into account the contribution of the nuclear spins in the paramagnetic state of the electronic spin system which was neglected at lower T . The results reveal that $T = 340$ K is the highest temperature where the oscillations exist in ZF- μ^+ SR data of AgRuO₃. Indeed, the μ^+ SR spectrum at $T = 340$ K (blue squares in Fig. 11a) displays a weak oscillation with frequency $\nu_0 = 7.25 \pm 0.75$ MHz extracted from the fit (red line). The FFT and fit analysis of the data at $T = 342.5$, 345, 347.5 and 350 K reveal no oscillations and are well reproduced by using only Kubo-Toyabe and nonoscillating terms. The depolarization of the asymmetry decreases progressively in the ZF- μ^+ SR data at $T = 342.5$, 345 and 347.5 K, suggesting a volume-wise destruction of the magnetic state with increasing magnetic disorder. The muon polarization is fully recovered at $T = 350$ K.

The extracted frequencies are plotted as a function of temperature in Fig. 13. The observed temperature dependence can be compared with that of the Ru ordered moment extracted from neutron diffraction measurements because the frequencies are proportional to the local fields. The inset of Fig. 13 shows the scaled frequencies plotted over the Ru ordered moment. The curves were matched at $T = 250$ K since this temperature is far from the critical region (vicinity of T_N) where neutrons and muons have different sensitivity due to the different time scales of the techniques. The comparison reveals a general good agreement of the temperature dependencies. The deviation above ≈ 310 K can be attributed to the fact that the ordered moment in a $k = 0$ magnetic structure may be underestimated in a fit analysis in the vicinity of T_N where the signal is weak.

To determine the Néel temperature T_N more accurately, and to address the issue of the critical dynamics, the temperature dependence of ν_0 was fitted by:

$$\nu(t) \propto (1 - (T/T_N))^\beta \quad (6)$$

where β is the critical exponent and the range of fit was $325 \text{ K} < T < 337.5 \text{ K}$. The resulting value $T_N = 340.5 \pm 0.5 \text{ K}$ is in excellent agreement with the Néel temperature revealed by magnetic susceptibility and other methods. However, the critical exponent $\beta = 0.27 \pm 0.02$ is considerably reduced from the conventional powers $\beta = 0.312$ [39], $\beta = 0.3485$ [40] and $\beta = 0.36$ [39] derived for the 3D Ising, 3D XY and 3D Heisenberg magnetic systems, respectively. Such a reduction, of various strength, can be attributed to the dominance of the two-dimensional rather than three-dimensional correlations and is often encountered in quasi-2D layered magnets (e.g. see Table A.1 in Ref. [41]). A possible explanation is the presence of long-range interactions which can affect and reduce the observed critical exponent from the theoretical predictions [42]. In particular, according to Ref. [42], $\beta = 0.27$ would correspond to a 2D magnet with a long-range interaction decaying as $\sim 1/r^{3.3}$. The presence of long-range interactions is consistent with the quasimolecular picture suggested by theory (see Sec. III G), since such orbitals typically generate long-range magnetic interactions [43].

In order to elucidate the possible nature of the observed features we have calculated the electrostatic potential in the $R\bar{3}c$ structure (Fig. 14). The energy landscape is quite uniform, with only two minima sufficiently deep to trap muons. They are located at the $6b$ and $6a$ positions, with rhombohedral coordinates $(0, 0, 0)$ and $(1/4, 1/4, 1/4)$ at the centers of the Ru_6 hexagons and in the middle between the vertical Ru-Ru bonds, respectively. In the neutron-determined magnetic $R\bar{3}'c'$ structure both sites have zero magnetic dipole field by symmetry. In reality, of course, the muons are shifted toward oxygens, and the calculation shows that stopping sites are $\approx 1.2 \text{ \AA}$ removed from the oxygens. For each of the two positions there are 6 equivalent stopping sites, corresponding to the number of surrounding oxygens.

At high temperature the muons might be able to hop among these six position; if this hopping rate is of the same order as the precession frequency, μSR signal will be greatly broadened and when the hopping rate becomes larger, the observed frequency will be reduced to zero, since the local fields averaged over six stopping sites cancels by symmetry. Possibly, this explains our observations at 125–200 K. However, the origin of the single mode observed at higher temperature is unclear at the moment. Indeed, neutron scattering does not reveal anything unusual in terms of the long-range magnetic moment at these temperatures. Moreover, our calculations suggest that the potential barrier between $(1/4, 1/4, 1/4)$ and $(0, 0, 0)$ stopping sites is large enough to prevent muon hopping between them at this temperatures. One possibility, suggested by the transport measurements dis-

cussed above, is that defect states may play a role. If at some characteristic temperature a particular kind of defects (say, Ru vacancies) change their charge state, they may provide new traps for muons, thus generating a new mode. However we do not have any direct experimental or theoretical evidence for this scenario. It worth mentioning that similar frequency splitting was previously observed in other quasi-2D magnets $\text{Sr}_2\text{CuO}_2\text{Cl}_2$ [44] and $\text{Ca}_{0.86}\text{Sr}_{0.14}\text{CuO}_2$ [45] where no related phase transitions were detected using neutron diffraction.

G. Electronic structure

We start with simple GGA calculations. Similar to SrRu_2O_6 , it is only possible to achieve convergence for a Néel AFM configuration (all nearest neighbors must be AFM ordered) [16, 17]. Other solutions such as ferromagnetic (FM), zigzag-AFM, or stripy-AFM do not survive and collapse to the nonmagnetic configuration. This demonstrates that AgRuO_3 cannot be described by a conventional Heisenberg Hamiltonian, due to the itinerant nature of its electronic structure. The magnetic moment on the Ru ion is $1.24 \mu_B$, roughly consistent with experiment. Similar to SrRu_2O_6 this reduction is not related to any covalency effects, but can be traced down to the formation of quasimolecular orbitals (QMO) [16, 17]

However, there is a difference between AgRuO_3 and SrRu_2O_6 . First of all, in AgRuO_3 in the nonmagnetic state the bands derived from the E_{2g} and E_{1u} QMO, rendering it metallic, see left panel in Fig. 15, while the nonmagnetic SrRu_2O_6 is a semiconductor with the band gap of 60 meV [16]. Accounting for the spin polarization in the (Néel-AFM) opens the gap of 80 meV in AgRuO_3 , see right panel in Fig. 15. This agrees with the experimental estimation of the activation energy of 29–188 meV from an Arrhenius fit of the electric resistance [12].

The overall band structures in AgRuO_3 and SrRu_2O_6 are similar and again indicates the presence of QMO [4,

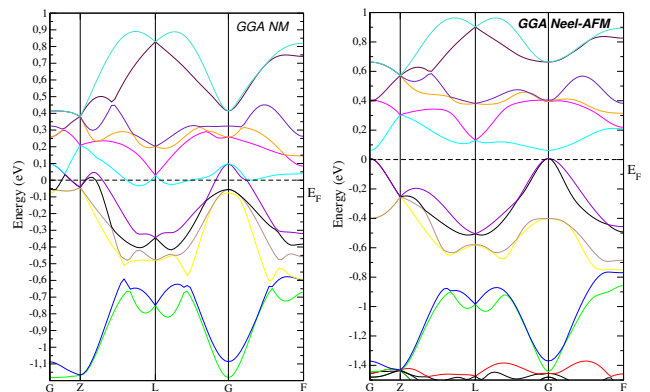


FIG. 15. Band structure as obtained in the GGA for nonmagnetic (left) and Néel-AFM (right) configurations as calculated in Wien2k [27].

17] in AgRuO_3 . However, the unit cell in AgRuO_3 is two times larger (different stacking along c) and therefore the number of the bands is twice that of SrRu_2O_6 . The lowest two bands are of B_{1u} symmetry, then four E_{2g} bands and then six bands two of which are of A_{1g} and four of E_{1u} symmetries.

The most important ingredient for the formation of QMO is the oxygen assisted hopping between unlike t_{2g} orbitals of nearest Ru ions, t'_1 (if these Ru ions are in the xy plane, then these will be $xz_1 - p_z - yz_2$ and $yz_1 - p_z - xz_2$ hopping, where 1 and 2 are ions indexes) [46]. The Wannier function projection procedure shows that $t'_1 = 0.28$ eV. There is also direct hopping between the same t_{2g} orbitals of nearest neighbor Ru ions (for the same xy plaquette this will be a hopping between xy orbitals) $t_1 = -0.27$ eV. This is different from SrRu_2O_6 , where $t'_1 \approx |2t_1|$ is responsible for the formation of the QMO [22]. Thus, the QMO are weaker in AgRuO_3 . Antiferromagnetism works against formation of QMO and therefore already on this stage we expect that the intraplane exchange interaction is stronger in AgRuO_3 .

We used the total energy GGA+SOC calculations (in the Néel-AFM state) to estimate the single ion anisotropy (SIA), which turns out to be the easy axis with $D = -12$ K, where $D = \delta E/M_z^2$ and M_z is z projection of the spin moment, δE is the energy difference between configurations with all spins lying in and perpendicular to the Ru-Ru plane. The corresponding total energy dependence on the spin canting angle is shown in Fig. 16. We see that the SIA constant, D , in AgRuO_3 is slightly larger than in SrRu_2O_6 ($D = -9$ K) [17].

The interlayer exchange interaction in AgRuO_3 is more tricky than in SrRu_2O_6 because of different stacking. Neighboring Ru layers are shifted with respect to each other as shown in Fig. 6. As a result the the shortest interplanar Ru-Ru bond (5.28 Å) for every Ru lead either to the plane below or to the plane above. However, because of the Néel order in the planes, the net interaction between the neighboring plane is always the same for all planes and can be described by one net exchange constant. We have calculated it to be $J_\perp = 2$ K, which is much smaller than in SrRu_2O_6 ($J_\perp = 10$ K). The sign of the interaction is positive, which automatically ensures the AFM stacking and the $R\bar{3}'c'$ structure.

Several times smaller interplanar coupling does not affect the magnetic properties much because it occurs logarithmically as a ratio to the very large intraplane exchange coupling. Since there is a single stable magnetic configuration one cannot recalculate J from energies of different magnetic solutions. Therefore we used the same strategy as was previously applied to SrRu_2O_6 : we calculated in GGA+SOC the energy dependence on the spin canting angle and fitted the result to the functional presented in Ref. [17]. This yields $J = 96$ K for Hamiltonian 3 or 255 K, if one uses magnetization instead of spins as was done in [17]. Corresponding data are shown in Fig. 16, which demonstrate that spins are rather soft in AgRuO_3 . If one still neglects this effect, then the spin-

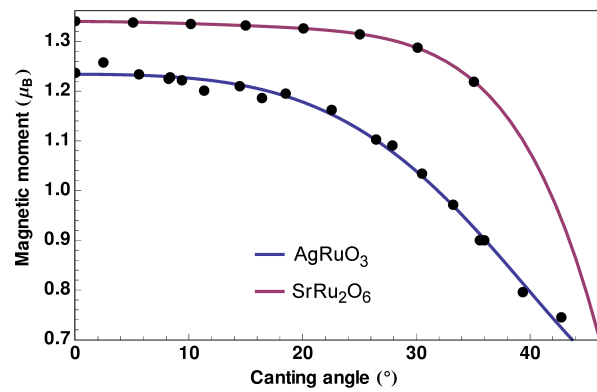


FIG. 16. Magnetic moment dependence on the spin canting angle (ϕ). Spins of two neighboring Ru ions are rotated in the plane of honeycomb lattice (so that angle between spins is 2ϕ). $\phi = 0$ corresponds to the Néel AFM structure.

wave theory can be used to estimate the Néel temperature according to [47, 48]. With calculated intra- and interplane exchange parameters we get $T_N = 304$ K, which is close to experimental 342 K. It should be mentioned that the calculated value of the intraplane exchange constant is also consistent with the Raman spectroscopy results.

IV. CONCLUSIONS

AgRuO_3 is a trigonal semiconducting ruthenium oxide with Ru^{5+} species in honeycomb [Ru_2O_6] layers. It shows a Néel-type antiferromagnetic order below 342(3) K (335–344 K, depending on the different experimental probes). The strongly anisotropic magnetic susceptibility (Fig. 1) is in agreement with the refinement of the AFM magnetic structure from powder neutron diffraction data, as well as with first principles calculation. The ordered Ru moments of $1.85(5) \mu_B$ lie (anti-)parallel to the c axis (magnetic point group $R\bar{3}'c'$; Fig. 6), slightly larger than the calculate moments of $1.27 \mu_B$, indicating a slightly more correlated character of Ru d -orbitals. Specific heat data show a second-order type transition at the Néel temperature and no further transitions, in agreement with the magnetic susceptibility measurements.

The Raman and zero-field muon spin rotation spectroscopy (μSR) data indicate subtle changes occurring between 150 K and 220 K. The apparent transport gap, calculated as $E_g(T) = T^2 d \log \rho(T)/dT$ shows a negligible activation gap up to ≈ 40 K, which then grows up to ≈ 70 K, reaching ≈ 25 meV, and then starts to decay, reaching ≈ 0 again at $T \sim 160$ K. After that it grows rapidly, reached ≈ 100 meV and after that remains constant up to the Néel temperature. This suggests that the intrinsic semiconducting gap is ≈ 100 meV, while the conductivity at low temperatures is dominated by a small number of carriers trapped and then thermally released by some defects.

At least one Raman mode, with the frequency $\approx 192 \text{ cm}^{-1}$, appears to be strongly coupled with these defects, and this coupling, as expected, is strongly temperature dependent. While all modes, including this one, are reproduced by the calculations, these calculations do not address the intensity of the Raman-allowed modes; we speculate that in the ideal crystal this mode is not visible without defect interference.

On a finer scale, one may discuss two potential energy scales. Indeed, the changes in the Raman spectra occur at $T \approx 170 \text{ K}$. This temperature is roughly in the middle of the crossover region ($125 \text{ K} < T < 200 \text{ K}$) identified in the ZF- μSR data, above which only a single oscillation mode is observed. Also, at about the same temperature the activation gap from electrical conductivity saturates. It is tempting to conclude that there are two energy scales, possibly associated with the two trapping sites, one of the order of 15–170 K, and the other 200–225 K.

Interestingly, these defects states do not contribute to bulk properties like the magnetic susceptibility and specific heat. The linear term in the low- T specific heat ($\gamma' = 5.6(1) \text{ mJ mol}^{-1} \text{ K}^{-2}$) is sizable but not uncommonly large for a polycrystalline sample of an insulating oxide. This corroborates our picture that defects, but not

changes in the basic electronic system of the compound, are responsible for the observed spectroscopic effects.

ACKNOWLEDGMENTS

We thank S. Scharsach and M. Schmidt for the DSC measurements and M. Baenitz and C. Shekhar for some measurements (not shown) in the early stage of this study. A.K.S. acknowledges the Department of Science and Technology (DST), India. S.P. acknowledges DST for an Inspire Fellowship. I.I.M. acknowledges support from the U.S. Department of Energy through grant #DE-SC0021089. E.V.K. and S.V.S. thank the Russian Foundation for Basic Researches (grants 20-32-70019 and 20-32-90073) and the Russian Ministry of Science and High Education via program ‘Quantum’ (grant AAAA-A18-118020190095-4) and contract 02.A03.21.0006. B.L. acknowledges support from the Deutsche Forschungsgemeinschaft (DFG) through project B06 of the SFB 1143 (ID:247310070). This work is partially based on experiments performed at the Swiss Muon Source $S\mu\text{S}$, Paul Scherrer Institute, Villigen, Switzerland.

-
- [1] A. Banerjee, J. Yan, J. Knolle, C. A. Bridges, M. B. Stone, M. D. Lumsden, D. G. Mandrus, D. A. Tennant, R. Moessner, and S. E. Nagler, Neutron scattering in the proximate quantum spin liquid $\alpha\text{-RuCl}_3$, *Science* **356**, 1055 (2017).
- [2] R. D. Johnson, S. C. Williams, A. A. Haghhighrad, J. Singleton, V. Zapf, P. Manuel, I. I. Mazin, Y. Li, H. O. Jeschke, R. Valentí, and R. Coldea, Monoclinic crystal structure of $\alpha\text{-RuCl}_3$ and the zigzag antiferromagnetic ground state, *Phys. Rev. B* **92**, 235119 (2015).
- [3] S. A. J. Kimber, I. I. Mazin, J. Shen, H. O. Jeschke, S. V. Streltsov, D. N. Argyriou, R. Valentí, and D. I. Khomskii, Valence bond liquid phase in the honeycomb lattice material Li_2RuO_3 , *Phys. Rev. B* **89**, 081408R (2014).
- [4] S. V. Streltsov, Low-Dimensional Ruthenates with Honeycomb Lattice, *Phys. Metals Metallography* **119**, 1276 (2018).
- [5] Z. V. Pchelkina, S. V. Streltsov, and I. I. Mazin, Spectroscopic signatures of molecular orbitals on a honeycomb lattice, *Phys. Rev. B* **94**, 205148 (2016).
- [6] L. Šmejkal, R. González-Hernández, T. Jungwirth, and J. Sinova, Crystal time-reversal symmetry breaking and spontaneous Hall effect in collinear antiferromagnets, *Science Adv.* **6**, eaaz8809 (2020).
- [7] G. Koster, L. Klein, W. Siemons, G. Rijnders, J. S. Dodge, C. Eom, D. H. A. Blank, and M. R. Beasley, Structure, physical properties, and applications of SrRuO_3 thin films, *Rev. Mod. Phys.* **84**, 253 (2012).
- [8] G. Cao, S. McCall, M. Shepard, J. E. Crow, and R. P. Guertin, Thermal, magnetic, and transport properties of single-crystal $\text{Sr}_{1-x}\text{Ca}_x\text{RuO}_3$ ($0 < x < 1.0$), *Phys. Rev. B* **56**, 321 (1997).
- [9] I. I. Mazin and D. J. Singh, Electronic structure and magnetism in Ru based perovskites, *Phys. Rev. B* **56**, 2556 (1997).
- [10] A. P. Mackenzie, A Personal Perspective on the Unconventional Superconductivity of Sr_2RuO_4 , *J. Supercond. Nov. Magn.* **33**, 177 (2020).
- [11] A. Pustogow, Y. Luo, A. Chronister, Y.-S. Su, D. A. Sokolov, F. Jerzembeck, A. P. Mackenzie, C. W. Hicks, N. Kikugawa, S. Raghu, E. D. Bauer, and S. E. Brown, Constraints on the superconducting order parameter in Sr_2RuO_4 from oxygen-17 nuclear magnetic resonance, *Nature* **574**, 72 (2019).
- [12] B. E. Prasad, S. Kanungo, M. Jansen, A. C. Komarek, B. Yan, P. Manuel, and C. Felser, AgRuO_3 , a strongly exchange-coupled honeycomb compound lacking long-range magnetic order, *Chem. Eur. J.* **23**, 4680 (2017).
- [13] D. L. Duong, S. J. Yun, and Y. H. Lee, van der Waals Layered Materials: Opportunities and Challenges, *ACS Nano* **11**, 11803 (2017).
- [14] C. I. Hiley, M. R. Lees, J. M. Fisher, D. Thompson, S. Agrestini, R. I. Smith, and R. I. Walton, Ruthenium(V) Oxides from Low-Temperature Hydrothermal Synthesis, *Angew. Chemie Int. Ed. Engl.* **53**, 4423 (2014).
- [15] C. I. Hiley, D. O. Scanlon, A. A. Sokol, S. M. Woodley, A. M. Ganose, S. Sangiao, J. M. D. Teresa, P. Manuel, D. D. Khalyavin, M. Walker, M. R. Lees, and R. I. Walton, Antiferromagnetism at $T > 500 \text{ K}$ in the layered hexagonal ruthenate SrRu_2O_6 , *Phys. Rev. B* **92**, 104413 (2015).
- [16] D. J. Singh, Electronic structure and the origin of the high ordering temperature in SrRu_2O_6 ,

- Phys. Rev. B **91**, 214420 (2015).
- [17] S. Streltsov, I. I. Mazin, and K. Foyevtsova, Localized itinerant electrons and unique magnetic properties of SrRu_2O_6 , Phys. Rev. B **92**, 134408 (2015).
- [18] A. Hariki, A. Hausoel, G. Sangiovanni, and J. Kuneš, DFT+DMFT study on soft moment magnetism and covalent bonding in SrRu_2O_6 , Phys. Rev. B **96**, 155135 (2017).
- [19] S. Okamoto, M. Ochi, R. Arita, J. Yan, and N. Trivedi, Localized-itinerant dichotomy and unconventional magnetism in SrRu_2O_6 , Sci. Rep. **7**, 11742 (2017).
- [20] Y. S. Ponosov, E. V. Komleva, D. A. Zamyatin, R. I. Walton, and S. V. Streltsov, Raman spectroscopy of the low-dimensional antiferromagnet SrRu_2O_6 with large Néel temperature, Phys. Rev. B **99**, 085103 (2019).
- [21] H. Suzuki, H. Gretarsson, H. Ishikawa, K. Ueda, Z. Yang, H. Liu, H. Kim, D. Kukusta, A. Yaresko, M. Minola, J. A. Sears, S. Francoual, H.-C. Wille, J. Nuss, H. Takagi, B. J. Kim, G. Khaliullin, H. Yava, and B. Keimer, Spin waves and spin-state transitions in a ruthenate high-temperature antiferromagnet, Nature Mater. **18**, 563 (2019).
- [22] D. Wang, W.-S. Wang, and Q.-H. Wang, t_{2g} -orbital model on a honeycomb lattice: Application to the antiferromagnet SrRu_2O_6 , Phys. Rev. B **92**, 075112 (2015).
- [23] W. Tian, C. Svoboda, M. Ochi, M. Matsuda, H. B. Cao, J.-G. Cheng, B. C. Sales, D. G. Mandrus, R. Arita, N. Trivedi, and J.-Q. Yan, High antiferromagnetic transition temperature of the honeycomb compound SrRu_2O_6 , Phys. Rev. B **92**, 100404(R) (2015).
- [24] T. Marchandier, Q. Jacquet, G. Rousse, B. Baptiste, A. M. Abakumov, and J. Tarascon, Expanding the Rich Crystal Chemistry of Ruthenium(V) Oxides via the Discovery of BaRu_2O_6 , $\text{Ba}_5\text{Ru}_4\text{O}_{15}$, $\text{Ba}_2\text{Ru}_3\text{O}_{10}$, and $\text{Sr}_2\text{Ru}_3\text{O}_9(\text{OH})$ by pH-Controlled Hydrothermal Synthesis, Chem. Mater. **31**, 6295 (2019).
- [25] L. C. Chapon, P. Manuel, P. G. Radaelli, C. Benson, L. Perrott, S. Ansell, N. J. Rhodes, D. Raspino, D. Duxbury, E. Spill, and J. Norris, Wish: The New Powder and Single Crystal Magnetic Diffractometer on the Second, Neutron News **22**, 22 (2011).
- [26] J. Rodríguez-Carvajal, Recent advances in magnetic structure determination by neutron powder diffraction, Physica B **192**, 55 (1993).
- [27] P. Blaha, K. Schwarz, G. Madsen, D. Kvasnicka, and J. Luitz, WIEN2k, An Augmented Plane Wave + Local Orbitals Program for Calculating Crystal Properties (Technische Universität Wien), ISBN 3-9501031-1-2. (2001).
- [28] G. Kresse and J. Furthmüller, Efficient iterative schemes for *ab initio* total-energy calculations using a plane-wave basis set, Phys. Rev. B **54**, 11169 (1996).
- [29] P. E. Blöchl, Projector augmented-wave method, Phys. Rev. B **50**, 17953 (1994).
- [30] J. P. Perdew, K. Burke, and M. Ernzerhof, Generalized gradient approximation made simple, Phys. Rev. Lett. **77**, 3865 (1996).
- [31] N. G. Parkinson, P. D. Hatton, J. A. K. Howard, C. Ritter, F. Z. Chien, and M.-K. Wue, Crystal and magnetic structures of $\text{A}_2\text{YRu}_{1-x}\text{Cu}_x\text{O}_6$ with $\text{A} = \text{Sr}, \text{Ba}$ and $x = 0.05$ to 0.15 , J. Mater. Chem. **13**, 1468 (2003).
- [32] H. T. Stokes, D. M. Hatch, and B. J. Campbell, ISOTROPY Software Suite, <http://iso.byu.edu>, accessed September 12, 2019.
- [33] B. J. Campbell, H. T. Stokes, D. E. Tanner, and D. M. Hatch, ISODISPLACE: a web-based tool for exploring structural distortions, J. Appl. Crystallogr. **39**, 607 (2006).
- [34] See Supplemental Material at [URL will be inserted by publisher] for a table and three additional figures with Raman spectroscopy data.
- [35] P. G. Klemens, Anharmonic Decay of Optical Phonons, Phys. Rev. **148**, 845 (1966).
- [36] P. Knoll, C. Thomsen, M. Cardona, and P. Murugaraj, Temperature-dependent lifetime of spin excitations in $\text{RBa}_2\text{Cu}_3\text{O}_6$ ($R = \text{Eu}, \text{Y}$), Phys. Rev. B **42**, 4842(R) (1990).
- [37] H. Gretarsson, N. H. Sung, M. Höppner, B. J. Kim, B. Keimer, and M. Le Tacon, Two-Magnon Raman Scattering and Pseudospin-Lattice Interactions in Sr_2IrO_4 and $\text{Sr}_3\text{Ir}_2\text{O}_7$, Phys. Rev. Lett. **116**, 136401 (2016).
- [38] A. Suter and B. Wojek, Musrfit: A Free Platform-Independent Framework for μSR Data Analysis, Phys. Procedia **30**, 69 (2012).
- [39] S. T. Bramwell, P. Day, M. T. Hutchings, J. R. G. Thorne, and D. Visser, Neutron scattering and optical study of the magnetic properties of the two-dimensional ionic ferromagnets $\text{Rb}_2\text{CrCl}_3\text{Br}$ and $\text{Rb}_2\text{CrCl}_2\text{Br}_2$, Inorg. Chem. **25**, 417 (1996).
- [40] M. Campostrini, M. Hasenbusch, A. Pelissetto, P. Rossi, and E. Vicari, Critical behavior of the three-dimensional XY universality class, Phys. Rev. B **63**, 214503 (2001).
- [41] A. Taroni, S. T. Bramwell, and P. C. W. Holdsworth, Universal window for two-dimensional critical exponents, J. Phys.: Condens. Matter **20**, 275233 (2008).
- [42] M. E. Fisher, S. K. Ma, and B. G. Nickel, Critical Exponents for Long-Range Interactions, Phys. Rev. Lett. **29**, 917 (1972).
- [43] S. M. Winter, A. A. Tsirlin, M. Daghofer, J. van den Brink, Y. Singh, P. Gegenwart, and R. Valentí, Models and materials for generalized Kitaev magnetism, J. Phys.: Condens. Matter **29**, 493002 (2017).
- [44] L. P. Le, G. M. Luke, B. J. Sternlieb, Y. J. Uemura, J. H. Brewer, T. M. Riseman, D. C. Johnston, and L. L. Miller, Muon-spin-rotation studies in single-crystal $\text{Sr}_2\text{CuO}_2\text{Cl}_2$, Phys. Rev. B **42**, 2182 (1990).
- [45] A. Keren, L. P. Le, G. M. Luke, B. J. Sternlieb, W. D. Wu, Y. J. Uemura, S. Tajima, and S. Uchida, Muon-spin-rotation measurements in infinite-layer and infinite-chain cuprate antiferromagnets: $\text{Ca}_{0.86}\text{Sr}_{0.14}\text{CuO}_2$ and Sr_2CuO_3 , Phys. Rev. B **48**, 12926 (1993).
- [46] I. I. Mazin, H. O. Jeschke, K. Foyevtsova, R. Valentí, and D. I. Khomskii, Na_2IrO_3 as a Molecular Orbital Crystal, Phys. Rev. Lett. **109**, 197201 (2012).
- [47] B. Schmidt, M. Siahatgar, and P. Thalmeier, Stabilization of Néel order in frustrated magnets with increasing magnetic field, EPJ Web of Conferences **40**, 04001 (2013).
- [48] E. Komleva, V. V. Y. Irkhin, I. Solovyev, V. M. Katsnelson, I. and S. Streltsov, V, Unconventional magnetism and electronic state in the frustrated layered system PdCrO_2 , Phys. Rev. B **102** (2020).

Supplemental Material for:
Magnetic and electronic ordering phenomena in the $[\text{Ru}_2\text{O}_6]$ honeycomb lattice
compound AgRuO_3

Walter Schnelle,* Beluvalli E. Prasad,† Claudia Felser, and Martin Jansen
Max Planck Institute for Chemical Physics of Solids, 01187 Dresden, Germany

Evgenia V. Komleva and Sergey V. Streltsov
*M. N. Miheev Institute of Metal Physics of Ural Branch of Russian Academy of Sciences, 620137 Ekaterinburg, Russia and
Ural Federal University, Mira St. 19, 620002 Ekaterinburg, Russia*

Igor I. Mazin
*Department of Physics and Astronomy and Quantum Science and Engineering Center,
George Mason University, 22030 Fairfax, Virginia, USA*

Dmitry Khalyavin and Pascal Manuel
ISIS Neutron and Muon Source, Rutherford Appleton Laboratory, Didcot OX11 0QX, U.K.

Sukanya Pal, D. V. S. Muthu, and A. K. Sood
Department of Physics, Indian Institute of Science, Bangalore 560012, India

Ekaterina S. Klyushina and Bella Lake
*Helmholtz Zentrum Berlin für Materialien und Energie, 14109 Berlin, Germany and
Institut für Festkörperphysik, Technische Universität Berlin, 10623 Berlin, Germany*

Jean-Christophe Orain and Hubertus Luetkens
*Laboratory for Muon-Spin Spectroscopy, Paul Scherrer Institute, 5232 Villigen PSI, Switzerland
(Dated: March 9, 2021)*

* walter.schnelle@cpfs.mpg.de

† Now at Department of Chemistry, RV Institute of Technology and Management, Bangalore, 560076, India

TABLE I. Experimentally observed frequencies at $T = 77$ K and calculated frequencies at 0 K along with assigned mode symmetries of the ($R\bar{3}c$) trigonal state of AgRuO_3 .

Mode index	Experimentally observed (cm^{-1}) (77 K)	Calculated (cm^{-1}) (0 K)	Assigned symmetry
M1	71.2	70.4	E_g
M2	92.5	87.1/90.3	A_{1g}/E_g
M3	175.9	179.0	A_{1g}
M4	193.0	198.1	E_g
M5	200.0	202.2	E_g
M6	311.4	303.7/309.1	E_g
M7	332.5	344.0	A_{1g}
M8	480.0	478.6	E_g
M9	495.0	484.1/486.2/499.7	E_g
M10	526.0	527.9	E_g
M11	552.3	557.3	A_{1g}
M12	595.8	579.5/580.1	A_1/A_{2u}

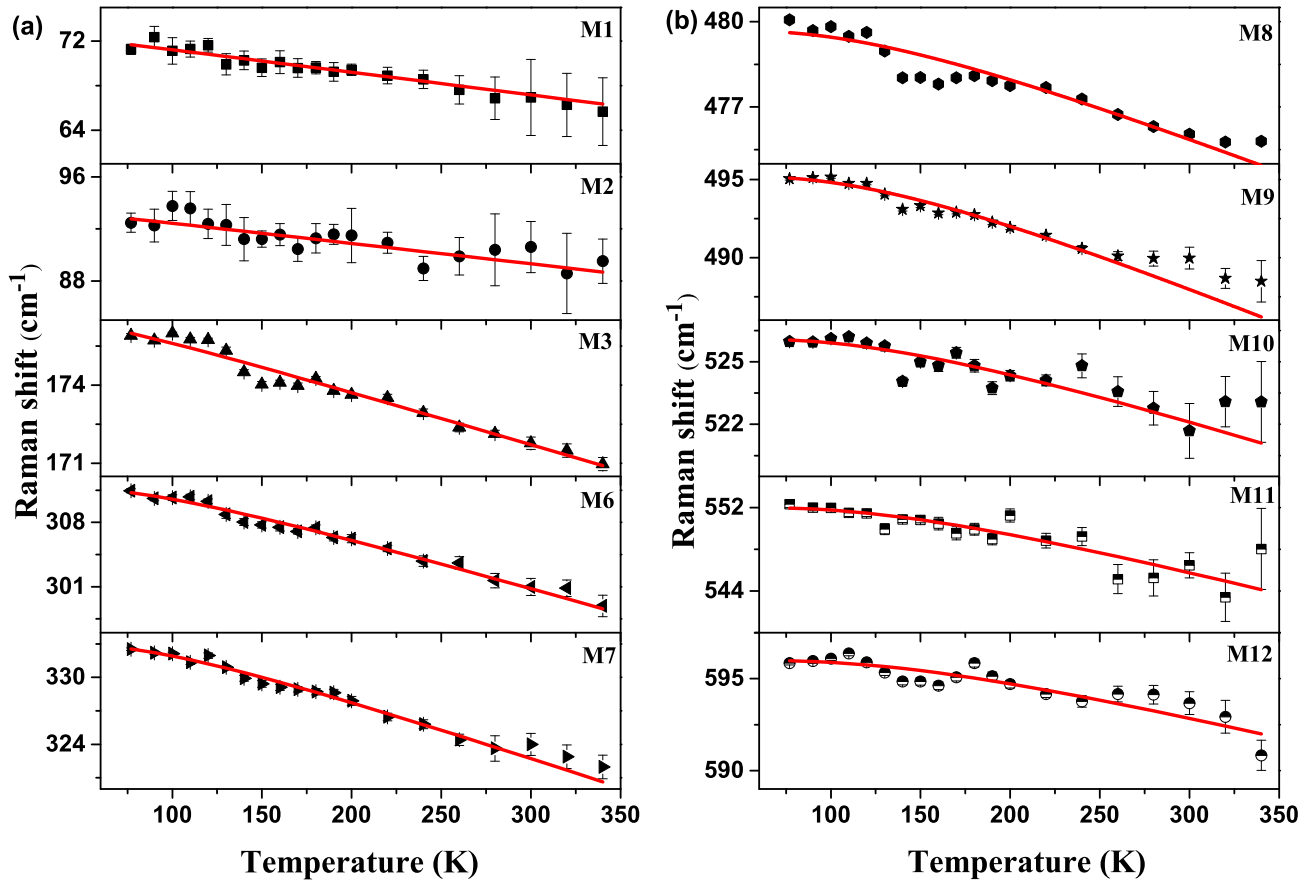


FIG. 1. Temperature dependence of phonon frequencies of the Raman modes of AgRuO_3 . The error bars are also displayed and are less than the size of the symbol when not shown. The red solid lines are fit to a simple cubic anharmonic model to the experimental data.

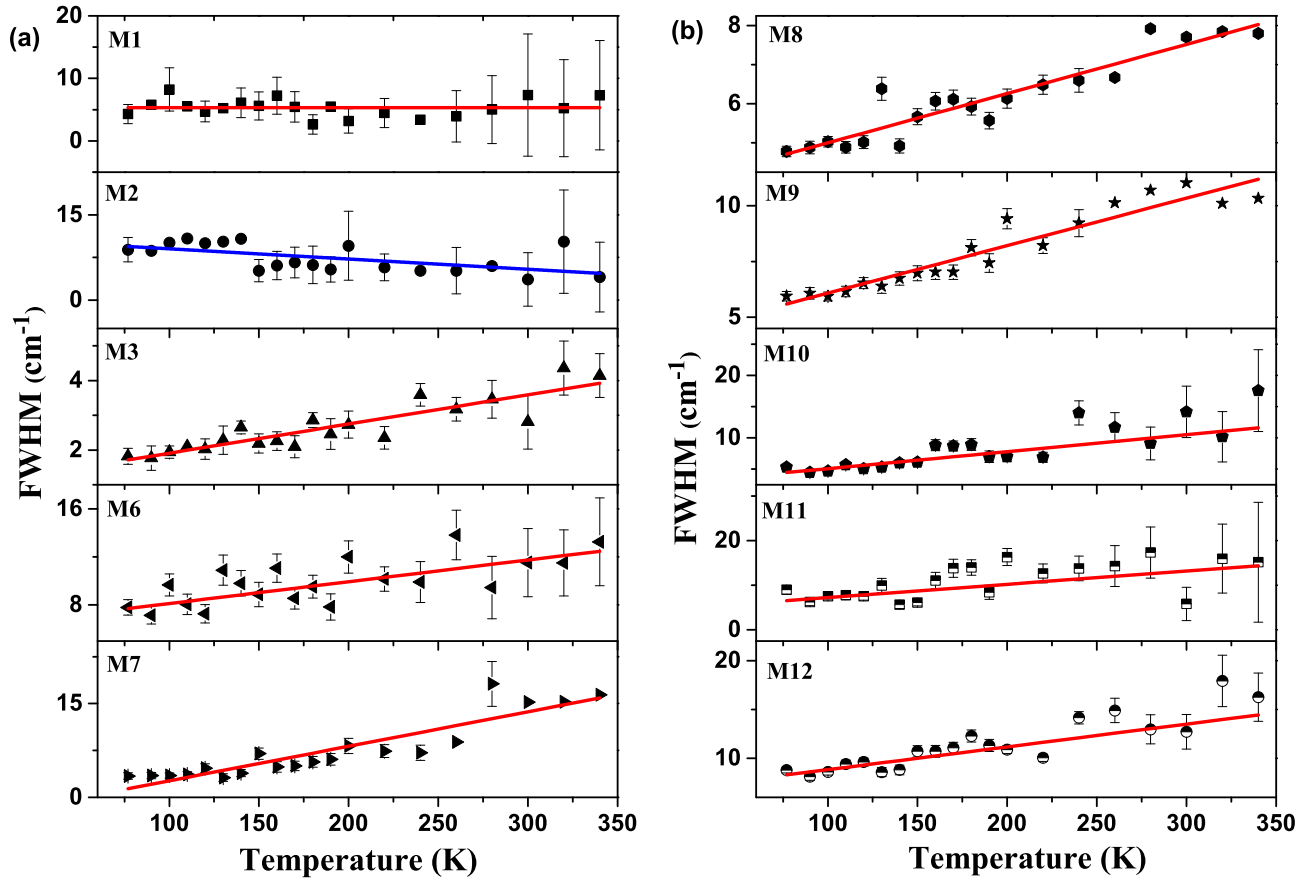


FIG. 2. Temperature dependence of phonon linewidths of the Raman modes of AgRuO_3 . The red solid lines are fit to a simple cubic anharmonic model to the experimental data. FWHM of the mode M2 remains almost constant and the solid blue line linear fit to the data.

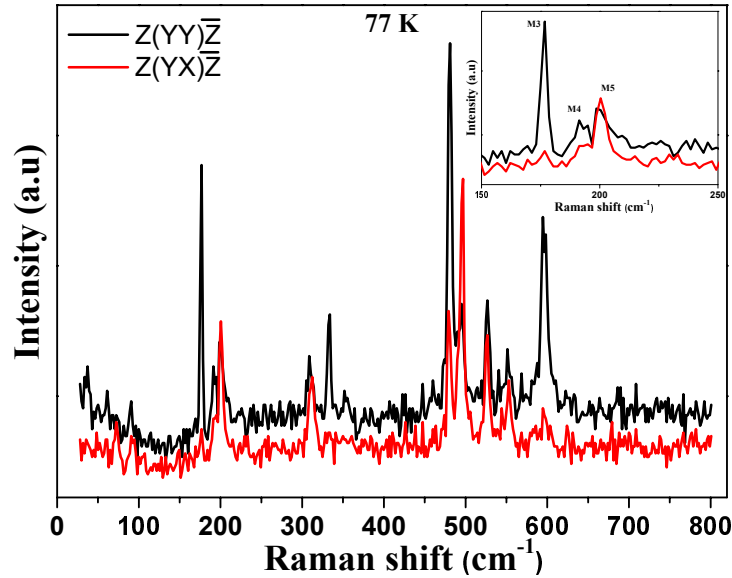


FIG. 3. Raman spectra of AgRuO_3 measured at $T = 77$ K in different polarization geometries. The inset shows zoomed-in spectra in the range $150\text{--}200\text{ cm}^{-1}$ confirming the presence of modes M4 and M5 in both parallel and crossed polarization configurations.